



Numerical modelling of the effects of foundation scour on the response of a bridge pier

Andrea Ciancimino¹ · Ioannis Anastasopoulos² · Sebastiano Foti¹ · Alessandro Gajo³

Received: 19 January 2022 / Accepted: 8 May 2022 / Published online: 22 June 2022
© The Author(s) 2022

Abstract

Foundation scour can have a detrimental effect on the performance of bridge piers, inducing a significant reduction of the lateral capacity of the footing and accumulation of permanent settlement and rotation. Although the hydraulic processes responsible for foundation scour are nowadays well known, predicting their mechanical consequences is still challenging. Indeed, its impact on the failure mechanisms developing around the foundation has not been fully investigated. In this paper, numerical simulations are performed to study the vertical and lateral response of a scoured bridge pier founded on a cylindrical caisson foundation embedded in a layer of dense sand. The sand stress–strain behaviour is reproduced by employing the Severn-Trent model. The constitutive model is firstly calibrated on a set of soil element tests, including drained and undrained monotonic triaxial tests and resonant column tests. The calibration procedure is implemented considering the stress and strain nonuniformities within the samples, by simulating the laboratory tests as boundary value problems. The numerical model is then validated against the results of centrifuge tests. The results of the simulations are in good agreement with the experimental results in terms of foundation capacity and settlement accumulation. Moreover, the model can predict the effects of local and general scour. The numerical analyses also highlight the impact of scouring on the failure mechanisms, revealing that the soil resistance depends on the hydraulic scenario.

Keywords Centrifuge modelling · Erosion · Foundation scour · Laboratory tests · Numerical modelling · Soil–structure interaction

Abbreviations

α	Constitutive parameter controlling the exponent of the hyperbolic stiffness relationship	d	Embedment depth
A	Multiplier in the flow rule	d_{50}	Mean grain size, corresponding to a passing percentage of 50%
A_G	Calibration parameter of the Hardin and Black (1966) equation for the small-strain shear modulus	D	Damping ratio
B	Constitutive parameter controlling the hyperbolic stiffness relationship	D_f	Diameter of the foundation
\mathbf{B}_0	Initial fabric tensor	D_R	Relative density
C_c	Curvature coefficient	ε_{ax}	Axial strain
C_u	Uniformity coefficient	ε_{vol}	Volumetric strain
		e	Void ratio
		e_{CS}	Void ratio at critical
		e_{max}, e_{min}	Maximum and minimum void ratio
		E_R	Constitutive parameter defining the fraction of G_0 used in computations
		ϕ'_{CS}	Critical state friction angle
		$F(e)$	Void ratio function
		FS_v	Vertical safety factor
		γ_c	Cyclic shear strain amplitude
		γ'	Soil unit weight under buoyancy
		g	Gravitational acceleration
		G_0	Small-strain shear modulus
		G_S	Secant shear modulus

✉ Andrea Ciancimino
andrea.ciancimino@polito.it

¹ Department of Structural, Geotechnical and Building Engineering, Politecnico Di Torino, Turin, Italy

² Chair of Geotechnical Engineering, ETH Zurich, Zurich, Switzerland

³ Department of Civil, Environmental and Mechanical Engineering, Università Di Trento, Trento, Italy

G_s	Specific gravity of the grains	V_{ult}^{num}	Vertical bearing capacity as obtained from the numerical simulations
h_{act}	Distance between the actuator and the bottom of the footing	V_{ult}^{exp}	Vertical bearing capacity as obtained from the centrifuge test
H	Horizontal load	w	Settlement
\mathbf{I}	Second-order unity tensor	w_{ult}	Ultimate settlement associated with the vertical capacity
k	Constitutive parameter defining the link between changes in state parameter and the current size of the yield surface	Ψ	State parameter
k_d	State parameter contribution in the flow rule	W_1	Weight of the deck
K	Coefficient of lateral earth pressure	W_2	Weight the column
$K_{r,m}$	Secant monotonic rocking stiffness	W_3'	Weight of the footing under buoyancy
K_v	Tangent vertical stiffness		
λ	Slope of the CSL		
μ	Interface friction coefficient		
m	Constitutive parameter controlling the deviatoric section of the yield surface		
M	Overturning moment		
M_{ult}	Ultimate moment capacity of the structure		
M_{ult}^{exp}	Ultimate moment capacity of the structure as obtained from the centrifuge tests		
M_{ult}^{num}	Ultimate moment capacity of the structure as obtained from the numerical simulations		
M_{base}	Moment exerted by the base resisting mechanism		
M_{sides}	Moment exerted by the sides resisting mechanism		
$\Delta M(\delta)$	Second-order moment		
M_{CS}	Stress ratio at critical state		
ν	Poisson's ratio		
n_G	Exponent of the Hardin and Black (1966) equation for the small-strain shear modulus		
p'	Mean effective stress		
p_{atm}	Atmospheric pressure		
p'_{CS}	Mean effective stress at critical		
$P - \delta$	Second-order effects		
q	Deviatoric stress		
q_{CS}	Critical state deviatoric stress		
q_{peak}	Peak deviatoric stress		
θ	Rotation of the structure		
r	Ratio of sizes of the strength surface and the critical state surface		
R	Size of the yield surface to the strength surface		
σ'_h	Horizontal effective stress		
σ'_v	Vertical effective stress		
u_{tot}	Total displacement		
Δu_w	Excess pore water pressure		
v	Specific volume, equal to $1 + e$		
v_{CS}	Specific volume at critical		
v_λ	Intercept of the CSL		
V	Vertical load		
V_S	Small-strain shear wave velocity		
V_{ult}	Vertical bearing capacity		

1 Introduction

At the design stage of a bridge, the performance of its components has to be carefully evaluated from the *hydraulic*, *structural*, and *geotechnical* points of view. In addition, it is essential to ensure the stability and functionality of the structure during its service life, which can evolve due to both structural damage or ageing and variation of the supporting conditions [2].

Several studies have shown that the majority of bridge failures are a consequence of extreme flood events [30, 63]. The presence of a structure in a channel constitutes an obstacle to the water flow, leading to the development of turbulences around piers and abutments. Such vortices increase the erosive power of the flow, which may locally exceed the shear strength of the riverbed gaining the energy to excavate and carry out the soil material. This phenomenon, usually termed *local scour*, keeps going on until local equilibrium is re-established [41, 49]. In addition, aggradation and degradation phenomena, together with the reduction of the channel section, may result in global erosion of the riverbed—*general scour*. This erosive process typically takes place also around large monopile foundations, such as the ones usually employed for offshore wind turbines, affecting significantly their lateral behaviour [38].

The detrimental impact of scour on the mechanical response of bridge piers is nowadays well-recognized (e.g. [2]). Nevertheless, as noticed by Brandimarte et al. [9] bridge failures due to natural hazards and, in particular, foundation scour seem to be increasing with time. This is partly due to the large number of recent extreme flooding events, becoming increasingly frequent as a consequence of climate changes. In addition, budgetary constraints often prevent the timely implementation of risk mitigation measures, leading to an increase in vulnerability to extreme

events [39]. As a consequence, the static and seismic responses of scoured foundations have to be re-assessed in the aftermath of major flood events.

In the state of practice, such assessment is typically performed through numerical analyses (e.g. [62]), often neglecting the hydraulic processes leading to foundation scour. However, as shown experimentally by Qi et al. [48] and Ciancimino et al. [15], the effects of general and local scour are markedly different. In addition, the assumed shape of the scour hole has been shown to have an impact on the predicted performance of the foundation [13]. Unfortunately, it is difficult to a priori define the most critical situation, especially when seismic analyses are performed. Consequently, it is essential to model the response of scoured foundations as realistically as possible.

In this study, the impact of scouring on the performance of a bridge pier supported on a cylindrical foundation embedded in a layer of dense Perth sand is investigated through numerical analyses. The simulations refer to the prototype bridge pier which was investigated through centrifuge modelling by Ciancimino et al. [15]. Nonlinear soil response is modelled employing the Severn-Trent constitutive model [20, 22, 23]. The model has been proven to be effective in predicting sand behaviour for a wide range of boundary value problems (e.g. [1, 37, 51]). The constitutive parameters are carefully calibrated on the basis of element tests of Perth sand samples. The calibration procedure is firstly performed by comparing the results of drained triaxial tests to the numerical predictions, obtained by imposing a “true” triaxial stress state on a single finite element. The procedure is then refined by modelling the laboratory tests as boundary value problems, thus including the effect of sample edge restraints. The numerical predictions are also compared to the results of resonant column tests, confirming the validity of the calibration procedure.

Finally, the carefully calibrated constitutive model is used to simulate a series of centrifuge model tests conducted at the ETH Zurich (ETHZ) Geotechnical Centrifuge Center (GCC), allowing a detailed comparison of numerical predictions to experimental results. The purpose of this comparison is twofold: (a) it allows the assessment of the reliability of the numerical simulations, serving as a validation of the numerical model, and (b) the combined use of numerical and experimental results provides validated insights on the mechanisms and the overall response of bridge piers, especially concerning the impact of scour on the failure mechanisms that develop in the soil around the foundation.

2 Characterization of the Perth sand

The soil used in the centrifuge model tests is a fine silica sand from Western Australia, close to Perth (termed hereafter, Perth sand) with a mean grain size $d_{50} = 0.23$ mm and a soil particle specific gravity $G_s = 2.65$, characterized by a uniformity coefficient $C_u = 1.79$ and a curvature coefficient $C_c = 1.26$. The limiting void ratios are $e_{\min} = 0.50$ and $e_{\max} = 0.87$. The reported values are based on previous experimental studies [10, 45], except for e_{\max} for which a slightly higher value is adopted [15].

The stress–strain behaviour of Perth sand is discussed herein in the light of new element tests. Specifically, isotropically consolidated drained (CID) and undrained (CIU) compression triaxial tests were carried out on loose and medium-dense samples to estimate the position of the critical state locus. In addition, a series of resonant column (RC) tests was conducted to measure the small-strain shear modulus G_0 and the modulus reduction and damping (MRD) curves as a function of the effective confining pressure p' . The main findings of the laboratory tests are summarized in the next sections. More details on the testing procedures and the analysis of the results can be found in Ciancimino [14].

2.1 Triaxial tests

The main objective of the laboratory investigation is to identify the critical state line (CSL) of Perth sand in both the $q - p'$ and $e - \log p'$ planes. Defining its position is not a trivial task, especially in volumetric terms. A dense (i.e. dilative) sand sample sheared in both drained and undrained conditions will eventually reach the critical state at large axial strains, beyond the limits given by the assumptions adopted to interpret the results of laboratory tests. Moreover, the potential development of shear bands implies the necessity of defining the void ratio locally, even if the sample is sheared under undrained conditions with zero global volumetric strains (e.g. [16, 60]). Conversely, a sample looser than critical tends to reach the critical state at low axial strains, without significant development of shear bands [16]. The void ratio of the sample is thus almost homogeneous throughout the specimen. Consequently, it was decided to mainly perform undrained tests on loose and medium-dense samples to study the position of the CSL, looking for total, or at least partial, liquefaction.

2.1.1 Experimental programme and testing procedures

The tests were carried out by using the triaxial testing apparatus of the Geotechnical Laboratory of Politecnico di

Torino, specifically developed for testing sand samples under stress or strain control [12].

The specimens were prepared through the moist tamping method by adding a 5% weight of water to obtain loose, homogeneous samples with a diameter of 70 mm and a height of 140 mm. The sand was placed in a standard latex membrane (0.25 mm thick) applied via vacuum against the wall of a cylindrical split mould and levelled up to the desired height using a flat-bottom tamper. The procedure was repeated for 10 layers until the total specimen was created. After preparation, the samples were firstly saturated until B-values [57] higher than 0.97 were obtained and subsequently consolidated isotropically up to the initial mean effective pressure p'_0 . Finally, they were sheared in compression under displacement control through a digital press at a constant rate of 5 mm/h. Stresses and strains were monitored with an acquisition frequency of 0.2 Hz.

To compute the deviatoric stress q , a cylindrical deformation of the specimen was assumed, according to the ASTM D7181-20 standard. Despite being valid for the preliminary test phases (saturation and consolidation), this assumption is not completely appropriate during shearing. Nevertheless, it was decided to assume an average q for consistency with the adopted volumetric ϵ_{vol} and axial ϵ_{ax} strains which are computed as average global values.

As summarized in Table 1, five triaxial tests were performed in total.

2.1.2 Results

The results of the triaxial tests are summarized in Fig. 1. The CIU tests are presented in terms of deviatoric stress q and excess pore water pressure Δu_w versus ϵ_{ax} , whereas for the CID test the results are presented in terms of q and ϵ_{vol} .

The first two undrained tests (TX-PoliTO-01 and 02) were performed on medium-dense samples with $e_0 \approx 0.7$, consolidated up to p'_0 of 100 and 200 kPa, respectively. A dilative behaviour, typical of sands slightly denser than critical, is identifiable: an initial increase of Δu_w up to the phase transformation is followed by a decrease of Δu_w down to negative values and a consequent significant

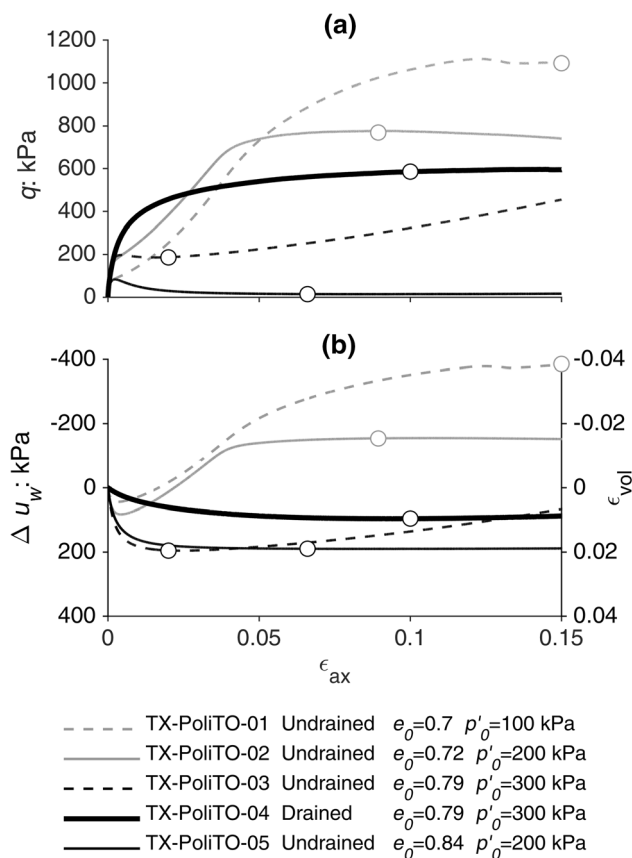


Fig. 1 Results of the triaxial tests carried out on loose and medium-dense samples: **a** deviatoric stress versus axial strain; **b** volumetric strain or excess pore water pressure versus axial strain. The circles in the plots represent the point identified as critical states

hardening (Fig. 1). In TX-PoliTO-01, the denser state of the soil and the lower p'_0 resulted in larger negative Δu_w compared to TX-PoliTO-02. The critical state condition for TX-PoliTO-01 is not clearly identifiable, even if the response seems to stabilize towards the end of the test. Conversely, in TX-PoliTO-02 the critical state seems to be reached for $\epsilon_{ax} \approx 0.08$, after which Δu_w and q are almost stable.

Tests TX-PoliTO-03 and 05 were conducted on loose samples ($e_0 = 0.79$ and 0.84) consolidated up to $p'_0 = 300$

Table 1 Summary of the triaxial tests carried out on loose and medium-dense samples of Perth sand

ID	Drainage	p'_0 : kPa	e_0	D_R : %	p'_{CS} : kPa	q_{CS} : kPa	e_{CS}
TX-PoliTO-01	Undrained	100	0.70	45.9	840*	1092*	–
TX-PoliTO-02	Undrained	200	0.72	40.5	611*	769*	–
TX-PoliTO-03	Undrained	300	0.79	21.6	168**	186**	0.79**
TX-PoliTO-04	Drained	300	0.79	21.6	496	586	0.77
TX-PoliTO-05	Undrained	200	0.84	8.1	13	14	0.84

*Critical State not clearly identified, point not used for the statistical regression

**Quasi-steady state

and 200 kPa, respectively. In TX-PoliTO-03, the sample experiences temporary liquefaction: a rapid increase of q is followed by a softening and temporary stabilization of Δu_w (Fig. 1). This condition is referred to as quasi-steady state and is followed by further hardening [60]. The question of whether this is an actual *material* behaviour or rather a *sample* behaviour caused by the limitations associated with the testing procedures is still debated (e.g. [65, 69]). Anyway, the two conditions (quasi-steady and steady state) are usually very close. The point was then included in the subsequent analyses for comparison purposes. Conversely, in TX-PoliTO-05 the very loose initial state of the sand leads to complete liquefaction of the specimen and an almost total loss of shear strength. After the peak, both q and Δu_w become stable and the sand reaches and maintains a clear critical state condition (Fig. 1).

The contractive behaviour of a loose ($e_0 = 0.79$) sample was investigated under drained conditions in test TX-PoliTO-04. The sand exhibits a monotonic increase of q until $\varepsilon_{ax} \approx 0.1$, after which q is almost constant and the critical state condition is reached (Fig. 1a). Such a trend is also visible in volumetric terms, where the sand experiences gradual contraction up to $\varepsilon_{vol} \approx 0.01$ (Fig. 1b). In this specific test, the initial state of the soil was probably really close to being critical, so small ε_{vol} developed during the shearing phase.

The critical state points (represented with circles in Fig. 1) are summarized in Table 1. For the two tests performed on medium-dense samples, the void ratios were not identified. Under undrained conditions, the tendency of medium-dense samples to dilate implies a decrease in the pore pressure until the critical state is reached (Fig. 1b). As observed by other studies (e.g. [26, 40]), the latter could lead to cavitation of the pore fluid and, in turn, to partially drained conditions. No values of void ratios at critical state are thus reported for these tests in Table 1 and the points are included just for comparison purposes.

2.1.3 Critical state line

The CSL of Perth sand in the $q - p'$ plane is presented in Fig. 2a, also reporting the quasi-steady state for comparison. The slope of the line is obtained through least-square regression and it is equal to a critical state stress ratio $M_{CS} = 1.23$. The corresponding critical state friction angle is $\varphi'_{CS} = 30.6 \pm 0.7^\circ$.

An estimate of the CSL in the volumetric plane is presented in Fig. 2b. Both the quasi-steady and the critical state points are reported, together with the paths followed by the samples during the compression phase. The CSL is described by adopting the equation proposed by Been and Jefferies [8]:

$$v_{CS} = v_\lambda - \lambda \cdot \ln p' \quad (1)$$

where v_λ and λ are two calibration parameters. By expressing p' in kPa, the parameters are 1.89 and 0.02, respectively. The position of the line appears to be reasonable and the intercept is quite close to the maximum specific volume associated with the loosest possible state. However, given the limited number of points used for the regression, the proposed equation is considered just an estimate of the CSL.

2.2 Resonant column tests

Resonant column tests were carried out to investigate the nonlinear response of Perth sand in a wide strain range. The tests were conducted using the combined RC and Torsional Shear device of the Geotechnical Laboratory of Politecnico di Torino [46], which is a modified version of the free-fixed type apparatus designed at the University of Texas at Austin [31]. The tests were performed and processed according to the prescriptions given in ASTM D4015-15.

2.2.1 Experimental programme and testing procedures

The RC tests were performed on dense samples with e_0 as close as possible to the centrifuge tests (0.55 – 0.60). With a diameter of 50 mm and a height of 100 mm, the specimens were prepared through the dry pluviation, aiming to achieve high relative densities while maintaining an acceptable degree of homogeneity. After preparation, the samples were saturated (in the case of undrained tests) and isotropically consolidated. The loading was imposed under load control, applying torques with increasing amplitude through an electromagnetic driving system. For a given amplitude, a wide range of frequencies was analyzed to identify the first torsional resonance frequency of the sample f_0 . The shear wave velocity V_s and the secant shear modulus G_s were computed by applying the theory of torsional wave propagation under steady-state conditions in a linear visco-elastic medium [50]. The damping ratio D was obtained by applying the free-vibration decay method. The dynamic parameters of the soil are referred to a cyclic shear strain amplitude γ_c equal to 2/3 of the maximum shear strain [29, 64].

A summary of the tests is given in Table 2. For each test, the experimental programme comprised several stages, each one consisting of initial isotropic consolidation to $p'_{0,i}$, followed by a full (i.e. from small to large strains) RC test performed in undrained mode. During the test, the eventual pore water pressure build-up was recorded. At the end of each stage, before starting a new consolidation phase, the drainage was opened to allow dissipation of Δu_w . Test RC-PoliTO-01 comprised 4 stages carried out at p'_0 ranging

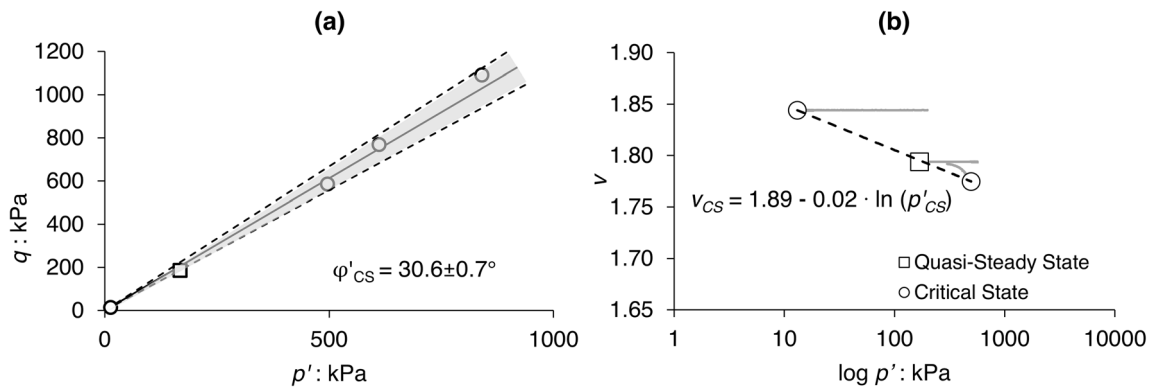


Fig. 2 Estimate of the CSL for the Perth sand in the **a** $q - p'$ and **b** $v - \log p'$ planes

from 25 kPa up to 200 kPa; 5 stages were conducted in test RC-PoliTO-02, with a maximum p'_0 of 400 kPa.

The procedure adopted for the first two tests allowed investigation of the influence of p' on the modulus reduction and damping (MRD) curves of Perth sand, similarly to previous studies (e.g. [43]). However, such a procedure is not appropriate to study the evolution of G_0 with confining pressure. When a sand sample is excited in undrained conditions above the volumetric threshold, it exhibits a pore pressure build-up. Consequently, during the dissipation phase, the sample experiences permanent changes in the microstructure and further densification [56].

A third experiment (RC-PoliTO-03) was performed on a dry sample, following a different 16-stages procedure. The first 10 stages (RC-PoliTO-03-A in Table 2) were performed at low strain amplitudes, so as not to exceed the linearity threshold, thus preventing any change in the structure of the sample. Such stages allowed the definition of G_0 evolution for confining pressures ranging from 25 to 800 kPa. When the maximum desired $p'_{0,i}$ was reached, a full (from small to large shear strains) RC test was carried out. The confining pressure was then progressively decreased in further stages (RC-PoliTO-03-B in Table 2), and for each stage, the MRD curves of the sample were obtained.

2.2.2 Small-strain shear modulus

The small-strain shear modulus G_0 of sand mainly depends on the actual state of the material. Hardin and Black [28] firstly pointed out this dependency, suggesting to express G_0 as a function of p' and e .

Figure 3 presents the experimental data in function of normalized confining pressure p'/p_{atm} , with superimposed the relationship of Hardin and Black [28], calibrated for this data set. The obtained A_G is 31.8 (with G_0 in MPa), which is in good agreement with values suggested for rounded sands, while for the exponent n_G a typical value of 0.5 is adopted for the sake of simplicity.

2.2.3 Modulus reduction and damping curves

The nonlinear behaviour of soils is usually represented through the MRD curves, exploiting the dependency of the visco-elastic parameters on the cyclic strain amplitude γ_c [53]. The main parameters affecting the MRD curves of sands are p' and particle gradation [42, 54]. The experimental curves are thus usually referred to p'_0 , corresponding to the initial value measured at the end of the consolidation phase. Nevertheless, p' can significantly change throughout testing under undrained conditions, due to the pore pressure build-up. It is then crucial to normalize each point of the MRD curves to the actual p'_i measured at resonance, in such a way to consistently compare results from different tests (see also [14]).

Table 2 Summary of resonant column tests (confining pressures and void ratios refer to the initial state for each i -th stage)

Test name	Nr. of stages	Drainage	Shear strain range	$p'_{0,i}$: kPa	$e_{0,i}$
RC-PoliTO-01	4	Undrained	Small-to-large	25, 50, 100, 200	0.60–0.59
RC-PoliTO-02	5	Undrained	Small-to-large	25, 50, 100, 200, 400	0.57–0.56
RC-PoliTO-03A	10	Drained	Small strains	25, 50, 100, 200, 300, 400, 500, 600, 700, 800	0.55–0.54
RC-PoliTO-03B	6	Drained	Small-to-large	800, 400, 200, 100, 50, 25	0.54–0.55

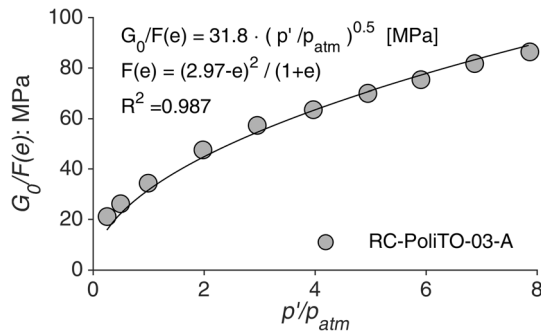


Fig. 3 Small-strain shear modulus of Perth sand in function of normalized confining pressure: calibration of the Hardin and Black [28] equation

The normalized MRD curves resulting from the RC tests are depicted in Fig. 8 (presented in the next section) as a function of p'_i . The increase of p'_0 leads to a shift of the MRD curves to the right, widening the almost linear range. In addition, an increase of p'_0 results in a decrease of the small-strain D . However, the influence of p' seems to be relevant for small pressures (< 100 kPa), becoming less significant at higher pressures consistently with previous findings (e.g. [54]).

3 Soil constitutive model

Nonlinear sand response is modelled employing the Severn-Trent sand model, as in the version proposed by Gajo [20]. Formulated within a bounding-surface approach, the original model [22, 23] can reproduce the stress–strain response of sands for a wide range of states with a single set of parameters. It relies on two surfaces: the strength surface and the yield surface, both defined through the Argyris et al. [4] criterion. The size of the strength surface is defined as a fraction of the critical state surface through ratio r :

$$r = 1 - k\Psi \quad (2)$$

where k is a constitutive parameter and Ψ is the state parameter, as proposed by Been and Jefferies [8]:

$$\Psi = v - v_\lambda + \lambda \ln p' \quad (3)$$

being v and p' indicative of the current state of the sand.

The size of the strength surface can then expand or shrink according to the evolution of the state of the material, while the position of its axis is fixed. The yield surface can undergo both isotropic and kinematic hardening and its size is defined as a fraction of the strength surface according to constitutive parameter R .

Although equivalent to the original one, the version employed herein [20] is based on the framework of the classical kinematic-hardening plasticity, adopting a

hyperelastic formulation to describe the soil behaviour inside the yield surface. Such formulation is modified as proposed by Argani and Gajo [4] to improve the rate of convergence for negligibly small confining pressures. At yielding, the magnitude of the plastic strain increment is related to the distance between the current stress state and an image stress state located on the strength surface through a hyperbolic relationship, based on constitutive parameter B . The stress–strain response is smoothed in the transition from the elastic to the elastoplastic zone through the introduction of a further constitutive parameter α . The model assumes the deviatoric associativity to link volumetric and distortional strain increments through the flow rule. The latter is defined based on two constitutive parameters: the multiplier A and a parameter k_d , defining the contribution of Ψ to the plastic flow.

The model was implemented by Gajo [21] as a user-defined material (UMAT) in the finite element (FE) code ABAQUS (Systèmes [59]).

3.1 Model calibration

The constitutive model is completely defined after thirteen constitutive parameters are calibrated. The parameters are summarized in Table 3 along with the values representative of the Perth sand response.

The first three parameters, v_λ , λ , and ϕ'_{CS} , define the position of the critical state surface and are selected on the basis of triaxial test results (see Fig. 2). In the present study, the inherent elastic anisotropy of the material (and its evolution) is neglected, so the initial fabric tensor \mathbf{B}_0 is assumed constant and equal to \mathbf{I} . The remaining parameters that control the elastic behaviour are derived by adopting Poisson's ratio $\nu = 0.2$ and G_0 defined through the Hardin and Black [28] equation (Fig. 3). Previous studies (e.g. [1, 23]) assumed a fraction E_R of G_0 instead of its full value as a strategy to better capture sand response under undrained conditions. The drawback of this strategy is that the drained behaviour, in the very small-strain range, could not be adequately reproduced. Bearing in mind that the target of this study is to reproduce the response observed in the centrifuge tests, it was decided to focus on the drained response, adopting G_0 . Consistently with this assumption, a small size of the yield surface $R = 0.01$ is selected (i.e. 1/100th of the strength surface).

Parameter m defines the deviatoric shape of the yield and strength surfaces through the Argyris et al. [4] criterion. A typical value of 0.8 is adopted to ensure the convexity of the surfaces. The remaining parameters are calibrated through a trial-and-error process, based on the results of the element tests. In particular, the calibration of A , B , k , and k_d is performed on the basis of drained triaxial

Table 3 Constitutive parameters of the severn-trent model for the Perth sand

Parameter	Description	Value
v_λ	Intercept of the CSL $p' = 1$ kPa	1.89
λ	Slope of the CSL	0.02
ϕ'_{CS}	Critical state friction angle	30°
m	Parameter controlling the deviatoric section of the yield surface	0.8
k	Link between changes in state parameter Ψ and current size of the strength and yield surfaces	2.6
A	Multiplier in the flow rule	0.65
k_d	State parameter contribution in the flow rule	1.8
B	Parameter controlling the hyperbolic stiffness relationship	0.007
α	Exponent controlling the hyperbolic stiffness relationship	1.2
R	Size of the yield surface with respect to the strength surface	0.01
E_R	Fraction of G_0 used in computations	1
ν	Poisson's ratio	0.2
\mathbf{B}_0	Tensor controlling the inherent anisotropy	\mathbf{I}

tests, resulting to $A = 0.65$, $B = 0.007$, $k = 2.6$, and $k_d = 1.8$. Parameter $\alpha = 1.2$ is defined considering nonlinear soil response, as observed from the RC tests.

3.2 Simulation of drained triaxial tests

The calibration of the constitutive model is performed mainly focusing on the results of drained tests. In particular, reference is made to test TX-PoliTO-04 (Table 1) and to the drained triaxial tests conducted by Bühler et al. [11] on dense Perth sand samples with e_0 very close to those measured in the centrifuge tests (Table 4).

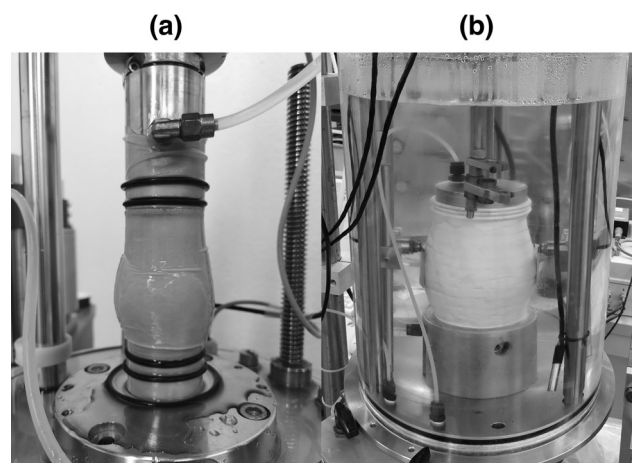
To interpret the test results, stresses and strains are computed in function of average external measurements, assuming cylindrical deformation of the specimen. Although this is a common assumption, it deserves an in-depth discussion. The effects of external boundary conditions can have a significant impact on the measured response. The rough end plates are known to impose non-uniform stress and strain fields within the specimen, which tend to lead to barrel-shaped deformation. Such a typical barrel shape was also observed in the performed Perth sand triaxial tests. Figure 4 compares the shape at failure of an initially denser (Fig. 4a) to a looser (Fig. 4b) than critical

Perth sand specimen. Strain localizations can readily be identified in the dense sample.

This issue has been analysed by several experimental and numerical studies (e.g. [44, 55]). The presence of the rough end plates leads to an apparent increase in shear strength (e.g. [35]). Moreover, the end-restraint prevents full development of volumetric strains throughout the specimen, which in the case of dense sand tends to localize within the shear bands [16]. As discussed by Sheng et al. [55], such boundary effects should be taken into account for proper constitutive model calibration. Following the notation introduced by Muraro and Jommi [44], the drained triaxial tests are simulated considering both *material behaviour* under true triaxial stresses and strains, and *sample behaviour*, treating the experiments as boundary value problems.

Table 4 Summary of the drained triaxial tests carried out by Bühler et al. [11] on dense Perth sand samples

ID	p'_0 : kPa	e_0	D_R : %
TX-ETH-01	50	0.52	93.7
TX-ETH-02	101	0.53	92.7
TX-ETH-03	200	0.53	93.2
TX-ETH-04	400	0.51	96.6

**Fig. 4** Typical barrel-shaped deformation observed on: **a** dense [11], and **b** loose sand specimens

A single CAX8R (i.e. 8-node axisymmetric quadrilateral, biquadratic displacement, reduced integration) element subjected to an initial isotropic triaxial state is sheared under drained conditions to simulate the *material behaviour* (Fig. 5a). Conversely, the *sample behaviour* is simulated by imposing the external boundary conditions on a quarter of the soil sample, modelled in axisymmetric conditions, and discretized as shown in Fig. 5b. The numerical model includes both the specimen and the steel top plate, which is assumed linear elastic with Young's modulus $E_S = 210$ GPa and Poisson's ratio $\nu = 0.3$. A rough interface (infinitely rigid in the normal direction) with friction coefficient $\mu = \tan \phi'_{CS}$ is introduced between the specimen and the top plate. Preliminary sensitivity analyses showed that in terms of global stresses and strains, the results are not sensitive to the assumed μ , neither on the mesh size [14]. After initial isotropic consolidation to p'_0 , the sample is sheared by applying an axial displacement to the top plate under drained conditions (i.e. imposing $\Delta u_w = 0$).

3.2.1 Material behaviour

In the simulations performed to evaluate the actual soil material behaviour, stresses and strains are uniform throughout a single element. The results can thus be directly extracted from the element integration points. The numerical results are compared to the measurements in Fig. 6a. The simulated deviatoric response of the dense samples is quite satisfactory for the entire range of ε_{ax} , although some small discrepancies can be observed. In

particular, the simulations predict slightly lower q_{peak} , after which a slower (compared to the experimental data) softening takes place. However, in terms of ε_{vol} the experimental results are captured only up to $\varepsilon_{ax} = 0.1$. For larger ε_{ax} , an apparent reduction of the ε_{vol} increment can be observed in the experimental measurements, which is attributed to strain localization (Fig. 4a).

Regarding the response of the initially looser than critical specimen, the comparison is satisfactory for the entire range of ε_{ax} in terms of progressive hardening of the material towards the critical state. In contrast to the dense sand experimental results, no significant strain localization is observed on initially loose samples (Fig. 4b). Consequently, in the case of loose sand, the interpretation of test results in terms of global quantities is considered reliable even at large ε_{ax} .

3.2.2 Sample behaviour

The sample behaviour is analysed considering *conventional* stresses and strains, computed for the entire specimen consistently with the procedures adopted to analyse the experimental results. Figure 6b compares the specimen simulation to the experimental results. In contrast to the single element analysis (material response), the experiments conducted on samples denser than critical are well captured for the entire range of ε_{ax} in terms of q_{peak} and post-peak softening. In addition, the predicted volumetric responses exhibit an *apparent* plateau at large strains, in excellent accord with the experimental results. No

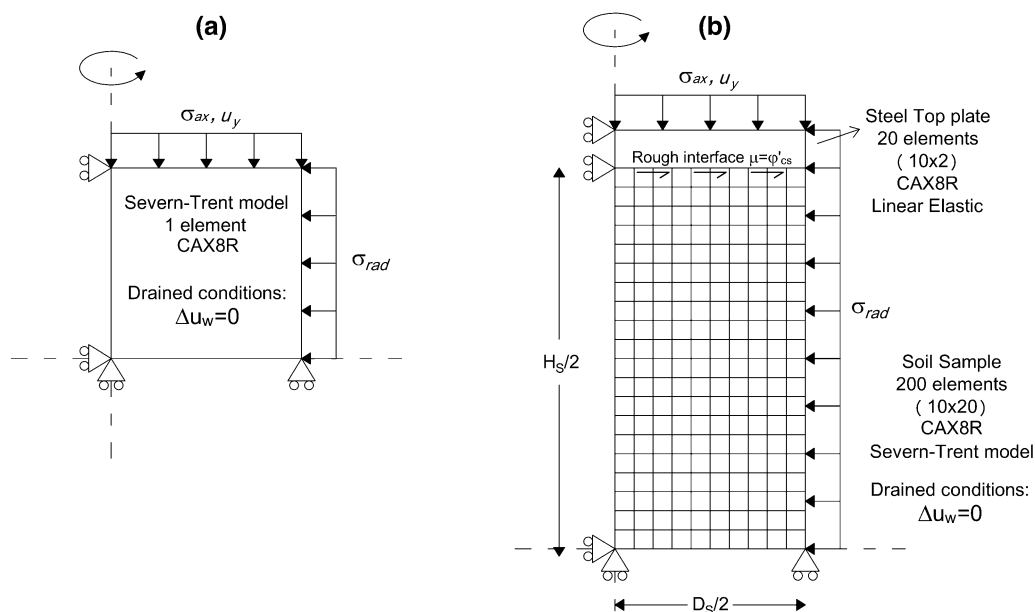


Fig. 5 Schematic illustration of FE models used to simulate: **a** material and **b** sample behaviour

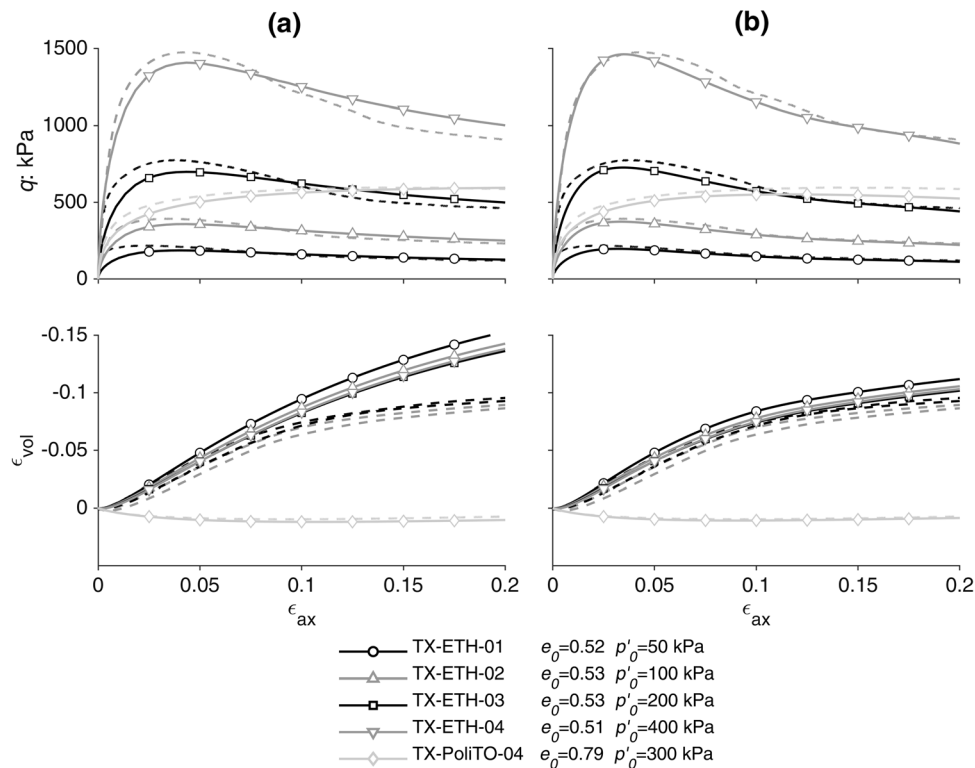


Fig. 6 Comparison of numerical predictions (solid lines) to experimental results (dashed lines) for: **a** material behaviour and **b** sample behaviour

significant differences are observed between material and sample response for the initially looser than critical specimen.

It is well known that strain localization is typically associated with a pathological dependency on the FE mesh. For this reason, the numerical simulations were repeated with different mesh refinements (not shown here for the sake of shortness) which led to substantially unchanged results in Fig. 6b [14].

Direct visualization of the differences between material and sample behaviour is offered in Fig. 7, which presents numerically predicted contours of void ratio e for a specimen initially denser (TX-ETH-04, Fig. 7a) and looser (TX-PoliTO-04, Fig. 7b) than critical, for global axial strain $\varepsilon_{ax} = 0.15$. The confinement offered by the steel end plates leads to a pronounced bulging of the initially dense specimen, whereas a smoother barrel shape is observed for the looser specimen. In the dense specimen, a clear strain localization can be observed, starting from about a quarter of the height and developing towards the middle of the specimen. In the elements located inside the shear band, e reaches quite a high value (0.81), in contrast to the so-called dead zones close to the top (and the bottom) of the specimen, where e is slightly higher than the initial one (0.51). In stark contrast, no significant nonuniformities can be observed in the e field of the loose sample.

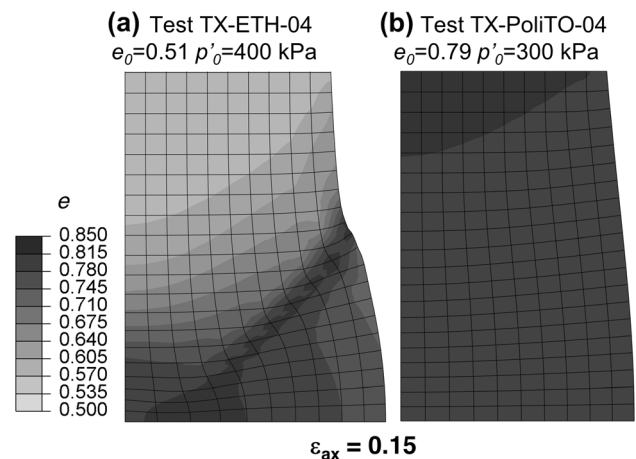


Fig. 7 Numerically computed contours of void ratio e distribution for a global axial strain $\varepsilon_{ax} = 0.15$ for: **a** specimen initially denser than critical and **b** initially looser than critical

The results are consistent with previous experimental and numerical findings, where specimens initially denser than critical presented an X-shape localization of shear deformations resulting in the formation of shear bands [16, 55]. Such shear bands formation implies a concentration of shear stresses, followed by faster softening of the global deviatoric response. On the other hand, it induces an *apparent* final plateau in the global volumetric strain response. The latter has to be interpreted as a manifestation

of strain localization, rather than the attainment of critical state condition for the entire specimen [16]. The sand attains critical state only locally, within the developing shear bands.

3.3 Modulus reduction and damping curves

Cyclic direct simple shear (CDSS) tests are simulated to compare the numerical predictions to the experimentally measured MRD curves. The numerical analyses are performed on a single C3D8R (8-node trilinear displacement, reduced integration) element. The analysis starts with an initial consolidation phase up to p'_0 , obtained by increasing the vertical effective stress σ'_z under oedometric conditions, followed by the shearing phase simulated by applying a cyclic horizontal displacement to the top nodes of the element under drained conditions.

The loading protocol consists of 10 cycles applied for 13 increasing displacement amplitudes, to adequately describe the range of shear strains investigated by the RC tests. The dynamic parameters of the soil are computed from the 10th load cycle for each displacement amplitude.

The numerical predictions are compared to the experimental data in Fig. 8. Although the present study focuses on the monotonic response of embedded foundations, the comparison is presented also in terms of damping curves for completeness. The smoothed variations of the curves with increasing γ_c are well captured by the constitutive model as well as their dependency on the confining pressure p'_0 . The only noticeable difference to the experimental results is a slightly faster decay of G_S/G_0 for γ_c ranging from 10^{-5} to 10^{-4} , and the corresponding overestimation of D at large strains, as typically predicted by nonlinear soil models.

4 Numerical simulations of centrifuge experiments

The thoroughly calibrated soil constitutive model is employed to simulate the centrifuge tests of Ciancimino et al. [15], focusing on the effects of scouring on the vertical and lateral response of a caisson foundation. Recognizing their ability to withstand severe earthquakes while suffering admissible damages in terms of permanent displacements and rotation [66], the seismic performance of caisson foundations has recently received growing attention (e.g. [24, 25]). However, the reduction of embedment due to scouring may lead to a substantial deterioration of their performance [68].

4.1 Centrifuge modelling

An idealized prototype bridge pier is considered, consisting of a single degree of freedom system supported on a cylindrical caisson foundation of diameter $D_f = 2$ m, embedded by $d = 2$ m in a layer of dense ($D_R \approx 80\%$) Perth sand (Fig. 9). To focus on the foundation response, the pier is modelled as a practically rigid slender structure. The physical model tests were conducted employing a decoupled hybrid approach [15]. The first step modelled in 1 g conditions the hydraulic process of local scour around the pier foundation, employing a miniaturized tidal generator (MTG) developed at ETHZ [33]. The morphology of the scour hole (Fig. 10) was acquired through 3D-scanning and used to 3D-print moulds to realistically reproduce its geometry in a centrifuge model, tested in the ETHZ drum centrifuge [58] to investigate under Ng the mechanical part of the problem. The tests were performed under drained conditions and checked through pore pressure transducers embedded in the sand.

The vertical response of the foundation was investigated through vertical push tests carried out at 100 g. The experimental setup consisted of an aluminium model of the foundation pushed with a constant velocity. The imposed

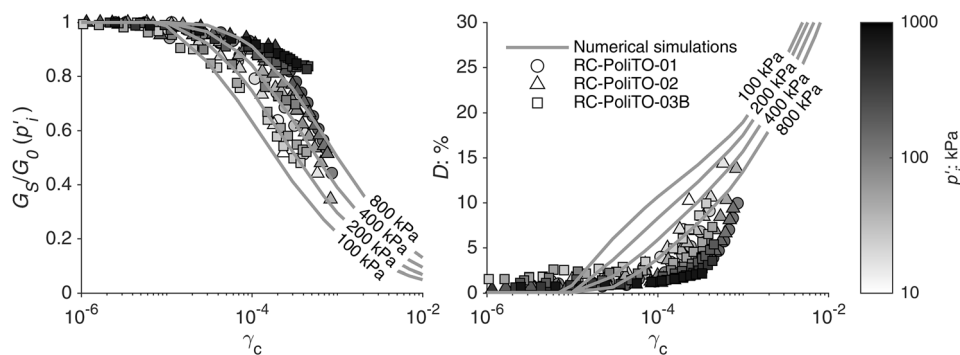


Fig. 8 Comparison of numerically predicted to experimentally measured MRD curves

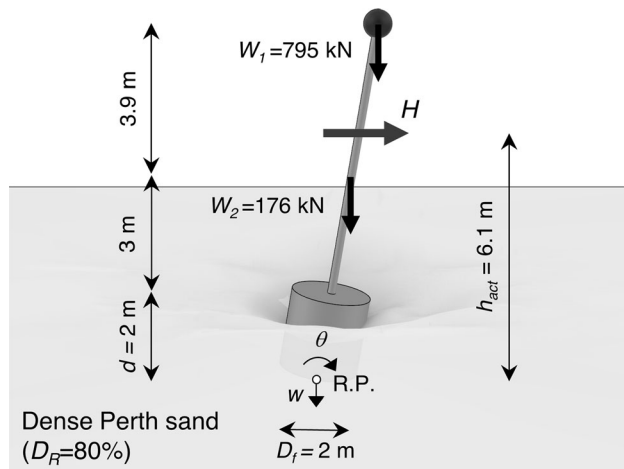


Fig. 9 Idealization of the prototype bridge pier of the centrifuge tests (R.P. stands for Reference Point)

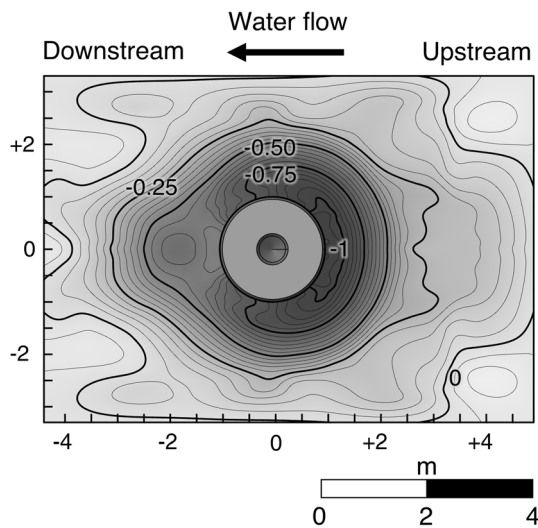


Fig. 10 Morphology of the local scour hole (in prototype scale) obtained through 3D-scanning of the 1 g physical model tested in the MTG [15]

vertical settlement w and the corresponding load V were measured to obtain the $V - w$ response of the foundation before and after local scour (tests V1_A and V2_A, respectively).

Displacement-controlled monotonic pushover tests were conducted at 50 g to study the lateral foundation response. The aluminium foundation was rigidly connected to the bridge pier, modelled using a practically rigid brass column, which was monolithically connected to a steel mass on the top representing the deck. The mass was selected so as to achieve a safety factor under purely vertical loading $FS_V \approx 8$, corresponding to a moderately loaded system. The FS_V is computed as follows:

$$FS_V = \frac{V_{ult} + W'_3}{W'_3 + W_2 + W_1} \quad (4)$$

where: W'_3 , W_2 , and W_1 are the weight of the footing accounting for buoyancy, the weight of the column, and the weight of the deck, respectively.

The lateral displacement was applied using an electric screw-jack actuator, connected to the model structure through a sliding hinge, equipped with a pinned connection, free to move in the vertical direction. The horizontal force was measured through a high-resolution load cell and used to obtain the overturning moment M , while the in-plane movement of the pier (in terms of imposed rotation θ and vertical settlement w) was monitored by three laser sensors.

The tests considered in the present study investigated the lateral monotonic response before foundation scour (test MH1), after local scour (tests MH2 and MH3), and after general scour (test MH5), corresponding to generalized erosion of a 1-m-thick soil layer (i.e. the average scour depth due to local scour). Under local scour conditions, the system response was studied along the transverse direction of the bridge, which is usually critical. Given the asymmetry of the scour hole along this direction (Fig. 10), it was necessary to carry out two tests, pushing the structure towards the upstream and downstream directions.

4.2 Numerical modelling aspects

Consistently with the target relative density of the study ($D_R = 80\%$), the models are initialized adopting a constant void ratio $e = 0.575$. The initial vertical effective stress σ'_v is computed considering a unit weight of the soil $\gamma' = 10.2 \text{ kN/m}^3$, and the horizontal effective stress σ'_h is obtained applying the coefficient of earth pressures at rest $K_0 = 0.35$, calculated applying Jaky's [32] equation with $\phi' = 40^\circ$. Consistently with the centrifuge tests, the analyses are performed under drained conditions.

An isotropic linear elastic constitutive law is adopted for the caisson, assuming the properties of aluminium, $E = 70 \text{ GPa}$, $\nu = 0.33$, and $\gamma = 27.5 \text{ kN/m}^3$. As in previous studies (e.g. [66, 67]), the caisson is modelled as “wished in place”. This simplification was done to focus on the effects of scouring but is also consistent with the preparation of the physical models. Moreover, the numerical simulations (and the centrifuge model tests) neglect the loading–unloading induced by progressive erosion of soil along the sides of the foundation. However, such a process is practically negligible, since the maximum thickness of eroded soil is 1 m, corresponding to $\Delta\sigma'_v \approx 10 \text{ kPa}$.

A purely frictional contact algorithm is employed to model the soil-caisson interface, thus allowing sliding and detachment. A “hard” pressure-overclosure relation is used

in the normal direction, while the interface response along the tangential direction is modelled with a “penalty” algorithm, assuming a friction coefficient $\mu = 0.23$. The latter is based on the results of a series of direct shear interface tests [52].

All numerical simulations are performed accounting for geometric nonlinearities to capture, in the lateral tests, the additional moment $\Delta M(\delta)$ given by second-order (i.e. $P - \delta$) effects. It is worth noting that large displacements are anyway expected to occur only along the (practically rigid) bridge pier. The nonlinear geometry has therefore practically no impact on the soil response.

4.3 Simulation of vertical push tests

As demonstrated in several previous studies (e.g. [3, 19, 27]), the lateral response of a foundation system is strongly dependent on its vertical loading, usually described by its safety factor against purely vertical loading FS_V . Therefore, simulating the response of the foundation under pure vertical loading is an essential first step.

The simulations of the vertical push tests consist of the following steps: (i) definition of initial equilibrium through a geostatic step; (ii) “wished in place” installation of the caisson; and (iii) vertical push under drained conditions. Consistently with the centrifuge tests, the analyses are performed under displacement control. As shown in Fig. 11, the $d = 2$ m embedded foundation extends 1 m above the ground surface (i.e. its total height is 3 m) to avoid numerical instabilities due to the “collapse” of soil along sides. The additional frictional resistance of this upper 1 m is practically negligible, and therefore the comparison is considered consistent, provided that this part of the foundation is modelled weightless.

A 2D axisymmetric FE model is employed to study the response of the foundation before and after generalized scour (Fig. 11a), while a 3D FE model is used to model the

foundation subjected to local scour (Fig. 11b) due to the irregular shape of the scour hole. Taking advantage of the symmetry along the direction of the water flow (Fig. 10), half of the domain is modelled in 3D to reduce computational cost. The dimensions of the discretized soil field match the geometry of the cylindrical strongboxes used in the centrifuge tests. The bottom nodes are fixed in the vertical direction, while the side nodes are free to move vertically. After preliminary sensitivity analyses [14], the element size is equal to 20 cm close to the foundation, progressively increasing towards the model boundaries. The 3D mesh is defined through a revolving procedure built-in ABAQUS, so as to be equivalent to the axisymmetric model. The discretization of the scour hole geometry is obtained through a bottom-up manual procedure, based on the actual morphology obtained from the MTG tests (Fig. 10).

To allow reaching very high-stress gradients in the soil close to the foundation avoiding the typical numerical issues related to volumetric and shear locking, the soil and foundation materials are modelled through CAX8R elements for the axisymmetric models and C3D20R (i.e. 20-node brick, triquadratic displacement, reduced integration) elements for the 3D model.

The numerical predictions (solid lines) are compared to the centrifuge test results (dashed lines) in Fig. 12 in terms of load-settlement ($V - w$) and tangent vertical stiffness-settlement ($K_V - w$) response. The comparison also includes the numerical results for generalized scour, for which no experimental result is available. The simulations predict adequately well the evolution of K_V with increasing w (Fig. 12b). The only noticeable difference is observed for the small-strain range ($w < 0.1$ m), where the experimentally measured K_V is significantly lower than the numerically predicted. With the increase of the imposed settlement w , the numerical curves converge towards the experimental measurements. Similar conclusions can be

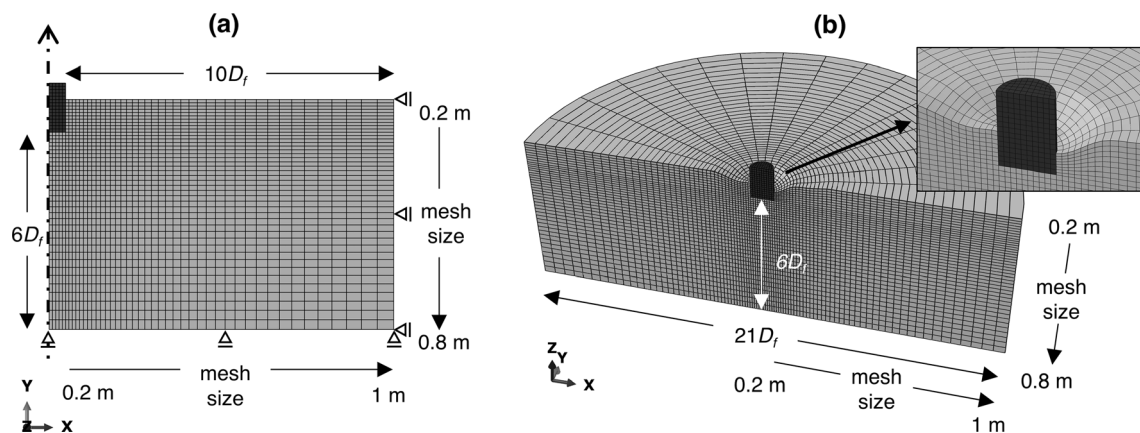


Fig. 11 FE modelling of vertical push tests: **a** 2D axisymmetric model and **b** 3D model of scoured foundation

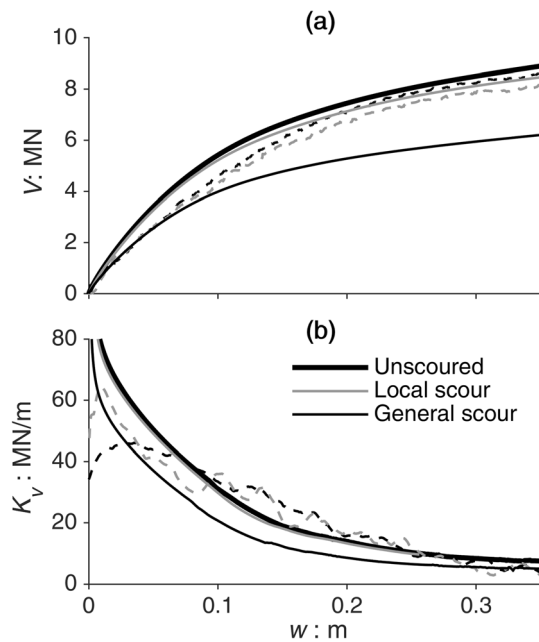


Fig. 12 Vertical loading of the caisson foundation before and after scouring. Numerical predictions (solid lines) compared to centrifuge test results (dashed lines): **a** load-settlement ($V-w$) response and **b** tangent vertical stiffness-settlement (K_v-w) response

drawn by the $V-w$ response (Fig. 12a), where the experimental V initially increases at a slower rate compared to the numerical prediction, progressively converging with the increase of w . A possible explanation of this discrepancy lies in the experimental procedure. To allow the caisson to freely settle during spinning up, the actuator arm is initially not in contact with the foundation. After attaining the target g -level the arm is pushed with constant velocity and contact is established. It is then possible that during the very first part of the vertical push, the contact is not yet perfect made, leading to larger measured w . The latter result in a lower initial value of K_v , which *apparently* increases at small strains. Nevertheless, soon after the contact is established, the issue is overcome and K_v starts to decrease. Therefore, the observed discrepancies in the small strain K_v may be due to such initial imperfect contact: “seating” effect.

As also observed in the centrifuge tests [15], a distinct plateau cannot be identified in the $V-w$ response (Fig. 12a). For $w < 0.1$ m, the response is only slightly nonlinear becoming strongly nonlinear with the increase w , as the failure mechanism is being mobilized. After the failure mechanism is fully developed, K_v tends to a residual (low, but nonzero) value. Consequently, the $V-w$ response exhibits a progressive hardening regime, suggesting the mobilization of a local shear failure mechanism rather than a general one [61]. In the absence of a clear plateau, the definition of the vertical ultimate load V_{ult} is

not obvious. When a foundation exhibits such a hardening regime, what effectively limits its V_{ult} is the accumulated settlement. Therefore, V_{ult} is defined herein as the load necessary to produce settlement $w_{ult} = 0.3$ m, which corresponds to a fairly large normalized settlement $w_{ult}/D_f = 15\%$. According to previous studies [3, 36], this point is practically coincident with the initiation of the hardening regime after which K_v is almost constant (Fig. 12b). Table 5 summarizes the V_{ult} obtained from numerical simulations and centrifuge tests. The observed differences can be quantified as follows:

$$\text{Diff}(\%) = \frac{V_{ult}^{\text{num}} - V_{ult}^{\text{exp}}}{V_{ult}^{\text{exp}}} \quad (5)$$

The comparison is very satisfactory, with a maximum difference of + 3.5% for the local scour condition. The numerical model successfully predicts the response of the caisson foundation under pure vertical loading and, most importantly, the (modest) effect of local scour. Local scour leads to a slight reduction of V_{ult}^{num} from 8.50 to 8.13 MN, due to the reduction of the effective overburden pressure in the soil below the foundation. The impact of general scour is much more pronounced in terms of both stiffness and bearing capacity (Fig. 12), leading to a 30% reduction of V_{ult}^{num} (from 8.50 to 5.95 MN).

4.4 Simulation of lateral pushover tests

The numerical predictions are compared to the results of the lateral pushover tests. A correction is applied to the experimental results to account for the effects of the radial gravity field on second-order additional moment $\Delta M(\delta)$ acting on the structure (see also [14]).

The numerical model includes a rigid massless column representing the pier, the caisson foundation, and the deck and pier masses, modelled as vertical loads applied at the corresponding centres of mass of the two parts (Fig. 9).

The simulations include four steps: (i) definition of initial equilibrium through a geostatic step; (ii) “wished in place” installation of the caisson foundation; (iii) activation of vertical loads; and (iv) horizontal pushover loading under drained conditions.

Table 5 Vertical ultimate load V_{ult} : comparison between numerical predictions and centrifuge test results

Condition	V_{ult} : MN		Diff: %
	Numerical simulations	Centrifuge tests	
Unscoured	8.50	8.23	+ 3.3
Local scour	8.13	7.85	+ 3.5
General scour	5.95	–	–

An increasing horizontal displacement is imposed on the rigid pier at a height $h_{act} = 6.1$ m to the base of the foundation, with the structure allowed to freely settle and rotate. The rocking response of the pier is calculated considering the in-plane rotation θ and the settlement w , computed concerning the reference point (i.e. the centre of the base of the caisson, Fig. 9). The horizontal force is used to compute the overturning moment M :

$$M = H \cdot h_{act} \tag{6}$$

The developed 3D FE model of half of the domain is shown in Fig. 13. Consistent with the centrifuge tests, the distance between the base of the caisson and the bottom boundary of the model is $3D_f$; the same applies to the distance of the caisson to model lateral boundaries. The latter has been shown to be sufficient to avoid boundary effects, in compliance with previous studies (e.g. [27, 67]). To reduce the computational cost, a mesh size varying from 20 to 40 cm is adopted up to a distance of $1D_f$ from the foundation, increasing to 80 cm further away. The soil and the caisson are modelled as previously described, while the pier is modelled as a discrete 2-node rigid beam (RB3D2) rigidly connected to the top of the caisson.

4.4.1 Results

The effects of scour on lateral pier-foundation response are analysed in terms of moment-rotation ($M - \theta$), settlement-rotation ($w - \theta$), and secant rocking stiffness-rotation ($K_{r,m} - \theta$) response. The numerical predictions (right) are compared to the experimental measurements (left) in Fig. 14 for the four hydraulic conditions examined: (a) before scour; (b) general scour; and (c) local scour

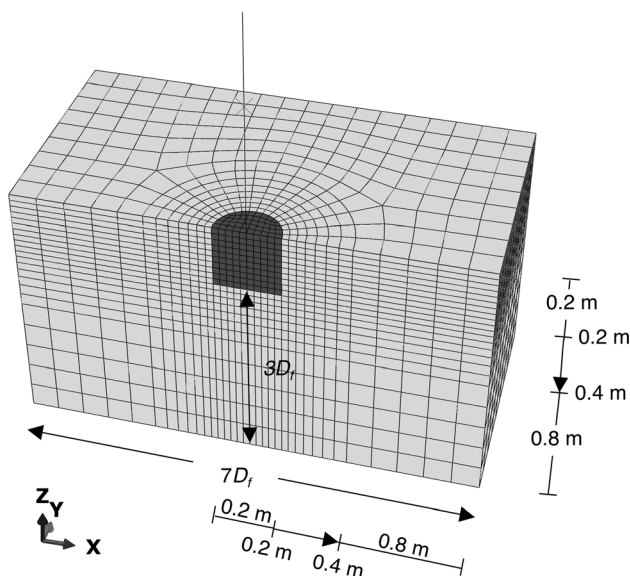


Fig. 13 3D FE model for lateral pushover tests: unscoured condition

around the pier, pushing the structure towards the upstream or downstream side.

The $M - \theta$ response (Fig. 14a) is used to define the lateral pushover capacity of the structures. For a given rotation θ , the actual resisting moment is theoretically given by the total moment M_{tot} acting on the foundation, including the additional moment $\Delta M(\delta)$ due to $P - \delta$ effects. However, the capacity of a foundation is usually defined as the maximum external load that the structure can withstand before suffering damage that could compromise the safety of the superstructure. Therefore, the moment capacity M_{ult} is defined according to the external $M - \theta$ response, thus implicitly considering second-order effects, as in previous studies (e.g. [19, 47]). To allow for direct comparison among the different conditions considered, M_{ult} is defined as the moment that develops for $\theta = 0.02$ rad. The latter coincides approximately with the rotation after which the $M - \theta$ curves start to decrease due to $P - \delta$ effects.

The moment capacity obtained from the numerical simulations (M_{ult}^{num}) and the centrifuge tests (M_{ult}^{exp}) are compared in Table 6, along with the corresponding FS_v , computed through Eq. (4) according to the V_{ult} reported in Table 5. The differences between numerical and experimental results are quantified as:

$$Diff(\%) = \frac{M_{ult}^{num} - M_{ult}^{exp}}{M_{ult}^{exp}} \tag{7}$$

The $M - \theta$ response (Fig. 14a) and the effects of scour are very well predicted by the numerical model up to fairly large θ . Their discrepancies range from -0.9% for the unscoured case to $+11.4\%$ for general scour. The effects of local scour are detrimental, leading to a reduction of M_{ult} of about 25% when the structure is pushed towards the upstream direction. The effect of general scour is even more pronounced, leading to 43% reduction.

The numerical prediction is satisfactory also in terms of $K_{r,m} - \theta$ response (Fig. 14c). General scour leads to a significant decrease of $K_{r,m}$ for the entire range of rotations. The reduction is less pronounced for local scour, but still significant. The reduction of $K_{r,m}$ is more obvious for small rotations. For $\theta = 0.001$ rad, $K_{r,m}$ is reduced from 115 MNm/rad before scouring, to 90 MNm/rad and 60 MNm/rad in the presence of local and general scour, respectively. This result is qualitatively consistent with what has been observed from monitoring data of real scoured bridges (e.g. [17, 34]).

Regarding the $w - \theta$ response (Fig. 14b), the simulation slightly overpredicts the dilative response of dense sand, partially compensating for the plasticity-induced settlements, leading to moderate uplifting of the caisson for $\theta > 0.02$ rad. However, it should be noted that the

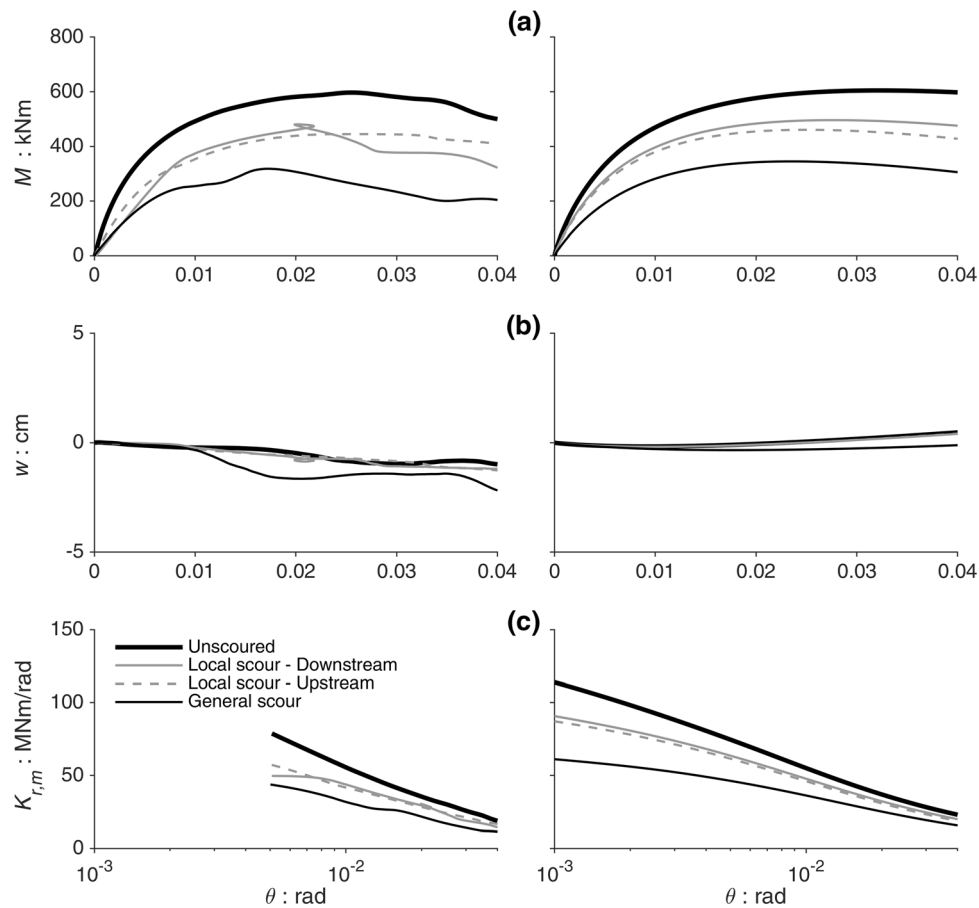


Fig. 14 Lateral pushover loading of the caisson foundation before and after scouring. Experimental measurements (left) compared to numerical predictions (right): **a** moment-rotation ($M - \theta$); **b** settlement-rotation ($w - \theta$); and **c** secant rocking stiffness-rotation ($K_{r,m} - \theta$) response

Table 6 Numerical predictions of the lateral pushover tests compared to experimental results

Condition	FS_v	M_{ult} : kNm		Diff: %
		Numerical simulations	Centrifuge tests	
Unscoured	8	577	582	-0.9
Local scour downstream	7.7	484	461	+ 4.9
Local scour upstream	7.7	455	439	+ 3.6
General scour	5.6	342	307	+ 11.4

numerical prediction is overall consistent with the experimental results. Both in the numerical simulations and the centrifuge tests, the response is neither sinking nor uplifting dominated. As already observed in previous experimental studies (e.g. [3]), such behaviour is reasonable for a moderately loaded foundation ($FS_v \approx 5 \div 10$) on dense sand, where the effects of the two mechanisms (dilation and plasticity-induced settlement) are comparable.

Under these conditions, the moderate effects of local scour on foundation bearing capacity (i.e. reduction of FS_v from 8.0 to 7.7) do not affect the accumulation of

settlement to a noticeable extent. In contrast, generalized scour leads to a moderate increase of the plasticity-induced settlement (Fig. 14b), resulting from the substantial decrease of FS_v to 5.6. Although general scour is not very relevant on the vertical response of the bridge pier analysed herein, it could become substantial for heavily loaded structures, where a similarly pronounced decrease of FS_v could lead to a transition to a sinking-dominated response.

4.4.2 Failure mechanisms

The total moment capacity of an embedded foundation is the result of two distinct resistance mechanisms: (a) base resistance (M_{base}) and (b) sides resistance (M_{sides}). In reality, the two mechanisms are coupled, but considering their effects separately allows for deeper insights into foundation response. The rotation of the structure leads to an increase of soil thrust (approaching passive conditions) along the pushing side of the foundation and a decrease along the opposite side (approaching active conditions). The corresponding sides' resistance M_{sides} is then the result of passive- and active-type failure mechanisms [18, 67]. Figure 15 compares the numerical failure mechanisms of the unscoured caisson to the cases of local (structure pushed towards the upstream direction) and general scour. The results are presented in terms of deformed mesh with superimposed total displacement u_{tot} (Fig. 15a) and void ratio e (Fig. 15b) contours for $\theta = 0.02$ rad.

The u_{tot} contours (Fig. 15a) reveal an almost purely rotational *scoop* failure mechanism, as it would be expected for pure moment loading of a rocking-dominated system [67]. Below the edge of the foundation on the pushing side, soil yielding induced by the base resistance mechanism leads to dilation, and consequently to an increase of the void ratio e of the initially dense sand (Fig. 15b). This effect is more pronounced when the foundation is subjected to general scour, due to the more pronounced reduction of FS_v ; the effect of local scour is much less pronounced. Active- and passive-type soil wedges can be observed along the sides of the caisson. While the active-type soil

wedge is clearly visible, the passive-type wedge does not seem to be fully mobilized.

To quantify the relative importance of the two resisting mechanisms, the total resisting moment is subdivided into M_{base} and M_{sides} in Fig. 16. M_{base} is computed by multiplying the normal nodal contact forces acting on the base of the caisson for the corresponding loading arm (measured at the reference point, R.P. in Fig. 9). M_{sides} is then obtained as the difference between the total moment (including second-order effects) and M_{base} .

For all the cases examined, M_{base} is almost fully mobilized for $\theta \approx 0.02$ rad (as revealed by the attained plateau), indicating that the corresponding failure mechanism is fully developed at this stage. As expected from the vertical push tests (Table 5), local scour does not significantly affect this mechanism (Fig. 16a). This is not the case for general scour, which leads to a significant (14%) reduction of M_{base} from 560 to 480 kNm. In stark contrast, M_{sides} exhibits more of a hardening response with increasing θ (Fig. 16b) for all cases examined. Interestingly, local and general scour have a markedly different effect on M_{sides} , despite the fact that almost the same depth of soil is removed. An impressive 83% reduction is observed for general scour, with M_{sides} (for $\theta = 0.02$ rad) decreasing from 180 to 30 kNm. Local scour also leads to a significant but less pronounced reduction, ranging from 51% ($M_{\text{sides}} = 89$ kNm) to 72% ($M_{\text{sides}} = 50$ kNm) when the structure is pushed towards the downstream and upstream side, respectively. These significant differences with respect to the direction of loading, which are function of the asymmetry of the scour hole, are only applicable to M_{sides} . For

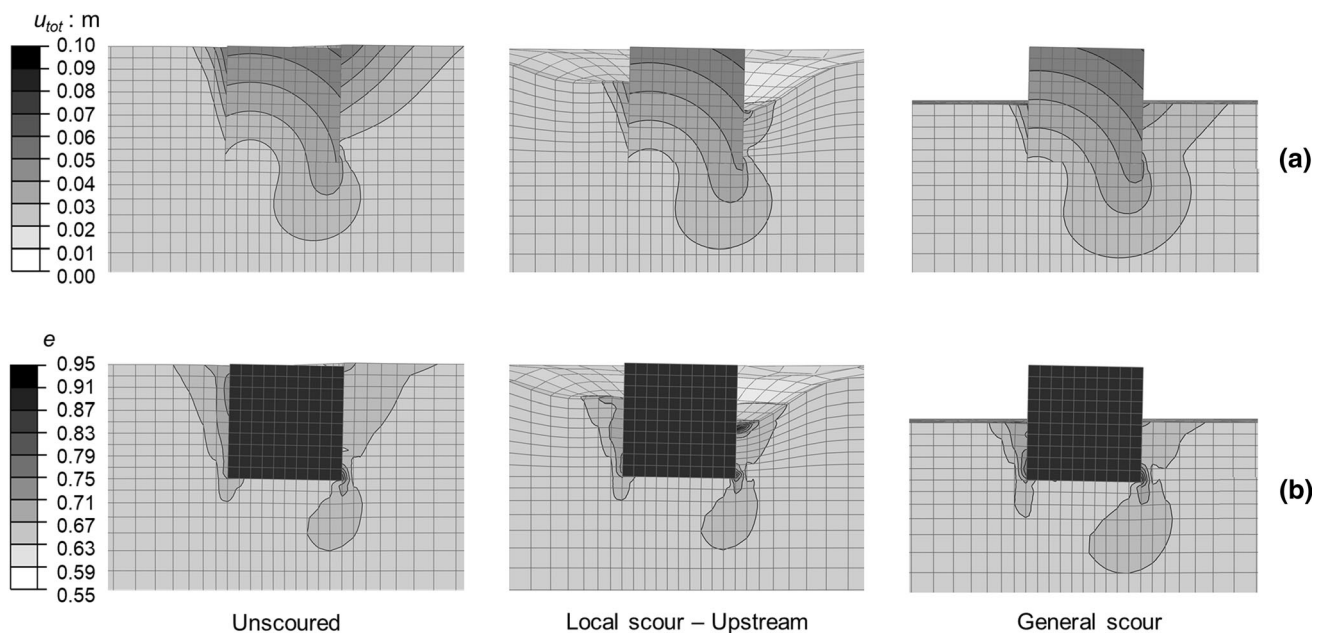


Fig. 15 Deformed mesh with superimposed contours of: **a** total displacement u_{tot} and **b** void ratio e ($\theta = 0.02$ rad)

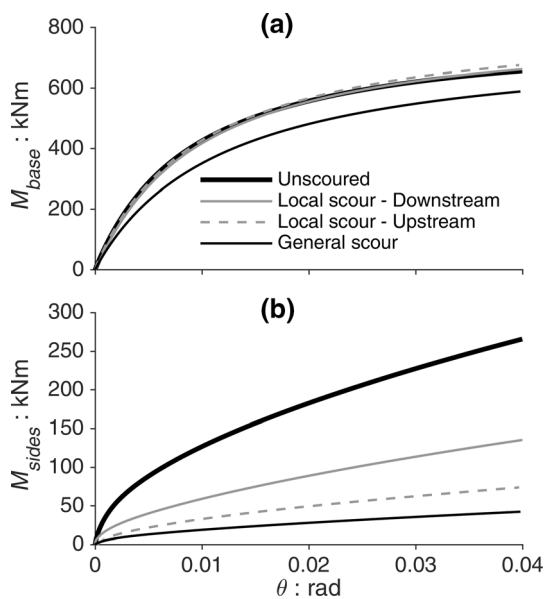


Fig. 16 Rocking response of the caisson foundation before and after scouring in terms of **a** base and **b** sides resisting moment-rotation curves

this specific caisson foundation, M_{base} is dominant, and therefore the effect on total resistance is limited. This is not necessarily the case for deeper embedded foundations, where the contribution of M_{sides} is usually dominant.

The effects of local and general scour on M_{sides} can be explained by looking at the stress fields in the soil elements along the sides of the foundation for $\theta = 0.02$ rad (Fig. 17). Under general and local scour, soil erosion leads to a substantial decrease of soil pressures along the pushing side (Fig. 17a, b) and, consequently, of M_{sides} (Fig. 16b). However, σ'_v (and consequently σ'_h) is substantially higher for the local scour condition due to the presence of the soil slopes of the scour hole. This explains the differences observed between the $M - \theta$ response obtained for the two hydraulic conditions (Fig. 16b).

The obtained earth pressure distributions are qualitatively consistent with the analytical solution proposed by Fröhlich [18]. The horizontal and vertical effective stresses follow a parabolic shape for all cases examined, with a maximum roughly at mid-height. Although the slope of the σ'_v distribution is almost equal to γ' close to the top-left edge of the foundation, it is substantially higher along its pushing side (Fig. 17a). As the caisson rotation increases, the sides of the caisson are no longer vertical and shear stress occurs in the soil close to the footing. As a result, the initially horizontal contact pressure also begins to rotate with its vertical component leading to the observed increase of σ'_v . As a consequence, the distribution of σ'_h along the pushing side is also increased (Fig. 17b), explaining the hardening response of M_{sides} observed in Fig. 16b. In contrast, σ'_h rapidly decreases to almost zero

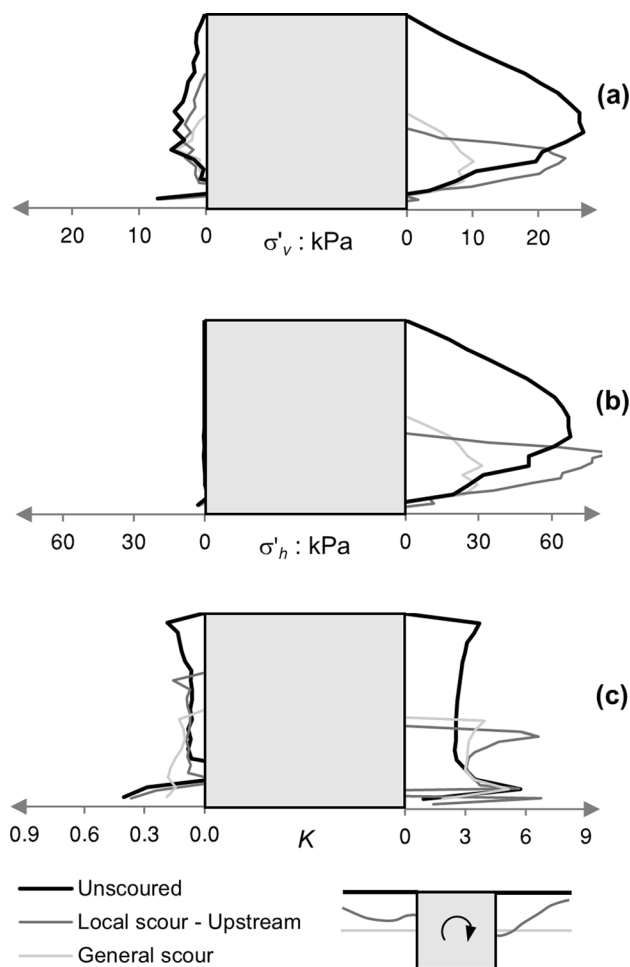


Fig. 17 Stress field in the soil elements along the sides of the foundation: **a** vertical effective stress σ'_v ; **b** horizontal effective stress σ'_h ; and **c** lateral earth pressure coefficient K ($\theta = 0.02$ rad)

along the opposite side of the caisson. The distributions of the coefficient of lateral earth pressure $K = \sigma'_h / \sigma'_v$ (computed locally for each integration point of the elements in contact to the foundation along the pushing direction) confirm these trends, which are the result of active- and passive-type failure mechanisms developing at the two sides of the foundation. While the active mechanism is fully mobilized for $\theta = 0.02$ rad ($K \approx 0.15 \div 0.20$), the passive mechanism along the pushing side appears to require further deformation to fully develop ($K \approx 3$).

5 Conclusions

This paper studied numerically the influence of foundation scour on the performance of a slender bridge pier supported on a cylindrical caisson foundation embedded in a layer of dense sand. The numerical simulations were conducted within the ABAQUS FE environment, employing the

Severn-Trent constitutive model [20, 22, 23] to simulate the nonlinear sand response. The model was initially calibrated on the basis of soil element tests, paying particular attention to the simulation of drained triaxial tests conducted on dense samples of Perth sand. The calibration process revealed the need to model the laboratory tests as boundary value problems due to stress and strain nonuniformities developing within the specimen.

The FE model was then validated against the results of centrifuge tests conducted at ETH Zurich [15]. The numerical predictions were shown to be in good agreement with the experimental results. Specifically, the numerical models are able to reproduce both the vertical and the horizontal response of the foundation in terms of capacity, stiffness, and settlement accumulation. Most importantly, the comparison is satisfactory when looking at the effects of local and general scour. This is of particular relevance, given the independent calibration of the model based on soil element tests, without any “fine-tuning” attempts to better match the centrifuge test results. It may therefore be concluded that it is possible to infer the mechanical consequences of foundation scour through numerical simulations, provided that the geometry of the problem is properly taken into account. The latter can be estimated based on available numerical and experimental studies of the hydraulic process of local scour around bridge piers (e.g. [41, 49]). Future mechanical studies should pay attention to the hydraulic conditions leading to foundation scour.

The numerical simulations have also provided new insights on the influence of foundation scour on the failure mechanisms developing in the soil around the caisson foundation. Generalized scour was shown to have a detrimental effect on vertical bearing capacity, leading to a reduction of FS_v from 8.0 to 5.6, whereas the effect of local scour is almost negligible. As a consequence, the general scour of the riverbed reduces both the sidewall and the base resistance mechanisms. Conversely, local scour only affects the sides’ resistance, exerted by the soil along the sides of the foundation. The latter is strongly asymmetric due to the morphology of the scour hole, which therefore plays an important role. For the specific foundation examined herein, such significant differences associated with the scour hole geometry, and therefore with the direction of loading, did not lead to any measurable effect in total moment resistance. This is because the examined cylindrical caisson is quite shallow ($D_f/d = 1$), and therefore the base resistance dominates the response. The effect of scour hole asymmetry can become significant for deeper and/or lightly loaded foundations, for which the sidewall contribution is expected to be more relevant.

Author contribution All authors contributed to the study conception and design. Material preparation, data collection, and numerical analyses were performed by Andrea Ciancimino. The first draft of the manuscript was written by Andrea Ciancimino, and all authors commented on previous versions of the manuscript. All authors read and approved the final manuscript.

Funding Open access funding provided by Politecnico di Torino within the CRUI-CARE Agreement. No funding was received to assist with the preparation of this manuscript.

Open Access This article is licensed under a Creative Commons Attribution 4.0 International License, which permits use, sharing, adaptation, distribution and reproduction in any medium or format, as long as you give appropriate credit to the original author(s) and the source, provide a link to the Creative Commons licence, and indicate if changes were made. The images or other third party material in this article are included in the article’s Creative Commons licence, unless indicated otherwise in a credit line to the material. If material is not included in the article’s Creative Commons licence and your intended use is not permitted by statutory regulation or exceeds the permitted use, you will need to obtain permission directly from the copyright holder. To view a copy of this licence, visit <http://creativecommons.org/licenses/by/4.0/>.

Data availability All data generated or analysed during the current study are available from the corresponding author upon reasonable request.

References

1. Abate G, Massimino M, Maugeri M, Wood DM (2010) Numerical modelling of a shaking table test for soil-foundation-superstructure interaction by means of a soil constitutive model implemented in a FEM code. *Geotech Geol Eng* 28:37–59
2. Alampalli S, Ettouney M (2008) Multihazard applications in bridge management. Paper presented at the tenth international conference on bridge and structure management, Buffalo, New York, October 20–22.
3. Anastasopoulos I, Kourkoulis R, Gelagoti F, Papadopoulos E (2012) Rocking response of SDOF systems on shallow improved sand: an experimental study. *Soil Dyn Earthq Eng* 40:15–33
4. Argani LP, Gajo A (2021) A new isotropic hyper-elasticity model for enhancing the rate of convergence of Mohr-Coulomb-like constitutive models and application to shallow foundations and trapdoors. *Comput Geotech* 132:103957
5. Argyris J, Faust G, Szimmat J, Warnke E, Willam K (1974) Recent developments in the finite element analysis of prestressed concrete reactor vessels. *Nucl Eng Des* 28:42–75
6. ASTM (2015) ASTM D4015–15: standard test methods for modulus and damping of soils by fixed-base resonant column devices. ASTM International, West Conshohocken, PA
7. ASTM (2020) ASTM D7181–20, standard test method for consolidated drained triaxial compression test for soils. ASTM International, West Conshohocken, PA
8. Been K, Jefferies MG (1985) A state parameter for sands. *Géotechnique* 35:99–112
9. Brandimarte L, Paron P, Di Baldassarre G (2012) Bridge pier scour: a review of processes, measurements and estimates. *Environ Eng Manag J* 11:975–989
10. Buchheister JA (2009) Verflüssigungspotenzial von reinem und siltigem Sand unter multiaxialer Belastung (in German). PhD dissertation, ETH Zurich.

11. Bühler F, Perrey S, Anastasopoulos I, Adamidis O, Sakellariadis L, Sieber M (2019) Element test characterisation of Perth sand. Master Project, ETH Zurich.
12. Carrera A (2008) Mechanical behaviour of Stava tailings. PhD dissertation, Politecnico di Torino.
13. Chortis G, Askarinejad A, Prendergast L, Li Q, Gavin K (2020) Influence of scour depth and type on p–y curves for monopiles in sand under monotonic lateral loading in a geotechnical centrifuge. *Ocean Eng* 197:106838
14. Ciancimino A (2021) Performance of caisson foundations subjected to flood-induced scour. PhD dissertation, Politecnico di Torino.
15. Ciancimino A, Jones L, Sakellariadis L, Anastasopoulos I, Foti S (2021) Experimental assessment of the performance of a bridge pier subjected to flood-induced foundation scour. *Géotechnique*. <https://doi.org/10.1680/jgeot.20.P.230>
16. Desrues J, Chambon R, Mokni M, Mazerolle F (1996) Void ratio evolution inside shear bands in triaxial sand specimens studied by computed tomography. *Géotechnique* 46:529–546
17. Foti S, Sabia D (2010) Influence of foundation scour on the dynamic response of an existing bridge. *J Bridge Eng* 16:295–304
18. Fröhlich H (1936) Beitrag zur Berechnung von Mastfundamenten (in German). Ernst & Sohn, Berlin
19. Gajan S, Kutter BL (2008) Capacity, settlement, and energy dissipation of shallow footings subjected to rocking. *J Geotech Geoenviron Eng* 134:1129–1141
20. Gajo A (2010) Hyperelastic modelling of small-strain stiffness anisotropy of cyclically loaded sand. *Int J Numer Anal Methods Geomech* 34:111–134
21. Gajo A (2017) Fortran subroutine in a format of user defined material (UMAT) of implementation of the Severn-Trent model.
22. Gajo A, Muir Wood D (1999) A kinematic hardening constitutive model for sands: the multi-axial formulation. *Int J Numer Anal Methods Geomech* 23:925–965
23. Gajo A, Muir Wood D (1999) Severn-Trent sand: a kinematic-hardening constitutive model: the q–p formulation. *Géotechnique* 49:595–614
24. Gaudio D, Rampello S (2019) The influence of soil plasticity on the seismic performance of bridge piers on caisson foundations. *Soil Dyn Earthq Eng* 118:120–133
25. Gaudio D, Rampello S (2020) Equivalent seismic coefficients for caisson foundations supporting bridge piers. *Soil Dyn Earthq Eng* 129:105955
26. Gawin D, Sanavia L (2010) Simulation of cavitation in water saturated porous media considering effects of dissolved air. *Transp Porous Media* 81:141
27. Gazetas G, Anastasopoulos I, Adamidis O, Kontoroupi T (2013) Nonlinear rocking stiffness of foundations. *Soil Dyn Earthq Eng* 47:83–91. <https://doi.org/10.1016/j.soildyn.2012.12.011>
28. Hardin BO, Black WL (1966) Sand stiffness under various tri-axial stresses. *J Soil Mech Found Div* 92:353–369. <https://doi.org/10.1061/JSFEAQ.0000865>
29. Hardin BO, Drnevich VP (1972) Shear modulus and damping in soils: design equations and curves. *J Soil Mech Found Div* 98:667–692
30. Imhof D (2004) Risk assessment of existing bridge structures. PhD dissertation, University of Cambridge.
31. Isenhowe WM (1979) Torsional simple shear/resonant column properties of San Francisco Bay mud. MS thesis, The University of Texas at Austin.
32. Jaky J (1944) The coefficient of earth pressure at rest (A nyugalmi nyomás tenezeje, in Hungarian). *J Soc Hung Eng Arch (Magyar Mernok es Epitesz-Egylet Kozlonye)* 355–358.
33. Jones L, Anastasopoulos I (2020) Miniaturised tsunami generator to model interaction of tsunami with coastal infrastructure. *Int J Phys Modell Geotech* 21:135–149. <https://doi.org/10.1680/jphmg.19.00021>
34. Kariyawasam KD, Middleton CR, Madabhushi G, Haigh SK, Talbot JP (2020) Assessment of bridge natural frequency as an indicator of scour using centrifuge modelling. *J Civil Struct Health Monit* 10:861–881
35. Kodaka T, Higo Y, Kimoto S, Oka F (2007) Effects of sample shape on the strain localization of water-saturated clay. *Int J Numer Anal Methods Geomech* 31:483–521
36. Kokkali P, Anastasopoulos I, Abdoun T, Gazetas G (2015) Static and cyclic rocking on sand: centrifuge versus reduced-scale 1 g experiments. In: *Geotechnical earthquake engineering: géotechnique symposium in print 2015*. ICE Publishing, pp 155–170
37. Kowalczyk P, Gajo A (2021) Influence of pore pressure on natural frequency wandering of structures under earthquake conditions. *Soil Dyn Earthq Eng* 142:106534
38. Li Q, Askarinejad A, Gavin K (2021) Impact of scour on lateral resistance of wind turbine monopiles: an experimental study. *Can Geotech J* 58:1770–1782
39. Macky G (1990) Survey of roading expenditure due to scour: a report for the Road Research Unit. Department of Scientific and Industrial Research, Hydrology Centre, Christchurch, New Zealand,
40. McManus K, Davis R (1997) Dilation-induced pore fluid cavitation in sands. *Géotechnique* 47:173–177
41. Melville BW, Coleman SE (2000) Bridge scour. Water Resources Publication, Highlands Ranch, CO, USA
42. Menq F-Y (2003) Dynamic properties of sandy and gravelly soils. PhD dissertation, The University of Texas at Austin.
43. Molina-Gómez F, da Fonseca AV, Ferreira C, Camacho-Tauta J (2020) Dynamic properties of two historically liquefiable sands in the Lisbon area. *Soil Dyn Earthq Eng* 132:106101
44. Muraro S, Jommi C (2019) Implication of end restraint in triaxial tests on the derivation of stress–dilatancy rule for soils having high compressibility. *Can Geotech J* 56:840–851
45. Nater P (2005) Belastungs- und Verformungsverhalten von geschichteten Bodensystemen unter starren Kreisfundationen. (in German). PhD dissertation, ETH Zurich.
46. Pallara O (1995) Comportamento sforzi-deformazioni di due sabbie soggette a sollecitazioni monotone e cicliche (in Italian). PhD dissertation, Politecnico di Torino.
47. Panagiotidou AI, Gazetas G, Gerolymos N (2012) Pushover and seismic response of foundations on stiff clay: analysis with p–delta effects. *Earthq Spect* 28:1589–1618
48. Qi WG, Gao F, Randolph MF, Lehane BM (2016) Scour effects on p–y curves for shallowly embedded piles in sand. *Géotechnique* 66:648–660
49. Richardson E, Davis S (2001) Evaluating scour at bridges: hydraulic engineering circular No. 18. Washington DC, USA
50. Richart FE, Hall JR, Woods RD (1970) Vibrations of soils and foundations
51. Rotisciani G, Miliziano S (2014) Guidelines for calibration and use of the Severn-Trent sand model in modeling cantilevered wall-supported excavations. *Int J Geomech* 14:04014029
52. Schwerzmann N (2019) Centrifuge study on pile foundations under axial loading. MS thesis, ETH Zurich
53. Seed H, Idriss I (1970) Soil moduli and damping factors for dynamic response analyses, Report no. EERC 70-10. Earthquake Engineering Research Center, University of California, Berkeley, California
54. Seed HB, Wong RT, Idriss I, Tokimatsu K (1986) Moduli and damping factors for dynamic analyses of cohesionless soils. *J Geotech Eng* 112:1016–1032
55. Sheng D, Westerberg B, Mattsson H, Axelsson K (1997) Effects of end restraint and strain rate in triaxial tests. *Comput Geotech* 21:163–182

56. Silver ML, Seed HB (1971) Volume changes in sands during cyclic loading. *J Soil Mech Found Div* 97:1171–1182. <https://doi.org/10.1061/JSFEAQ.0001658>
57. Skempton A (1954) The pore-pressure coefficients A and B. *Geotechnique* 4:143–147
58. Springman SM, Laue J, Boyle R, White J, Zweidler A (2001) The ETH Zurich geotechnical drum centrifuge. *Int J Phys Modell Geotech* 1:59–70
59. Systèmes Dassault (2020) ABAQUS/CAE software package
60. Verdugo R, Ishihara K (1996) The steady state of sandy soils. *Soils Found* 36:81–91
61. Vesic AB (1963) Bearing capacity of deep foundations in sand. Highway research record, vol 39
62. Wang Z, Dueñas-Osorio L, Padgett JE (2014) Influence of scour effects on the seismic response of reinforced concrete bridges. *Eng Struct* 76:202–214
63. Wardhana K, Hadipriono FC (2003) Analysis of recent bridge failures in the United States. *J Perform Const Facil* 17:144–150
64. Woods RD (1978) Measurement of dynamic soil properties. Paper presented at the ASCE geotechnical engineering division specialty conference, Pasadena, California, June 19–21
65. Yang J, Dai B (2011) Is the quasi-steady state a real behaviour? A micromechanical perspective. *Géotechnique* 61:175–183
66. Zafeirakos A, Gerolymos N (2014) Towards a seismic capacity design of caisson foundations supporting bridge piers. *Soil Dyn Earthq Eng* 67:179–197
67. Zafeirakos A, Gerolymos N (2016) Bearing strength surface for bridge caisson foundations in frictional soil under combined loading. *Acta Geotech* 11:1189–1208
68. Zhang C, Zhang X, Huang M, Tang H (2019) Responses of caisson-piles foundations to long-term cyclic lateral load and scouring. *Soil Dyn Earthq Eng* 119:62–74
69. Zhang H, Garga VK (1997) Quasi-steady state: a real behaviour? *Can Geotech J* 34:749–761

Publisher's Note Springer Nature remains neutral with regard to jurisdictional claims in published maps and institutional affiliations.